

# Theoretical and experimental investigation of the thermal resolution and dynamic range of CCD-based thermorefectance imaging

**Peter M. Mayer**

*Research Laboratory of Electronics, MIT, Cambridge, Massachusetts 02139, USA*

**Dietrich Lüerßen**

*Department of Physics, Mount Holyoke College, South Hadley, Massachusetts 01075, USA,  
and Research Laboratory of Electronics, MIT, Cambridge, Massachusetts 02139, USA*

**Rajeev J. Ram**

*Research Laboratory of Electronics, MIT, Cambridge, Massachusetts 02139, USA*

**Janice A. Hudgings**

*Department of Physics, Mount Holyoke College, South Hadley, Massachusetts 01075, USA*

Received September 11, 2006; revised November 7, 2006; accepted November 10, 2006;  
posted November 21, 2006 (Doc. ID 74893); published March 14, 2007

We demonstrate thermal imaging using a charge-coupled device (CCD) thermorefectance lock-in technique that achieves a record temperature resolution of 18 mK, 44 dB below the nominal dynamic range of the camera (from 72 to 116 dB) for  $10^5$  periods of measurement. We show that the quantization limit of the CCD camera does not set the lower bound on the precision of the technique. We present a theoretical description of the measurement technique, accounting for the effects of noise and nonideal analog-to-digital conversion, resulting in analytic expressions for the probability distribution function of the measured signals, and allowing for explicit calculation of resolution and error bars. The theory is tested against parametrically varied measurements and can be applied to other sampled lock-in measurements. We also experimentally demonstrate sub-quantization-limit imaging on a well-characterized model system, joule heating in a silicon resistor. The accuracy of the resistor thermorefectance measurement is confirmed by comparing the results with those of a standard  $3\omega$  measurement. © 2007 Optical Society of America

OCIS codes: 000.2170, 040.1520, 120.6780, 120.5700.

## 1. INTRODUCTION

Thermal imaging is important for many applications in physics and engineering, including device failure analysis and design optimization, thermal conductivity measurement, and thermal wave microscopy for the structural analysis of materials.<sup>1</sup> Well-established methods include infrared (IR) imaging,<sup>2</sup> scanning thermal microscopy,<sup>3</sup> and thermorefectance,<sup>4</sup> all of which have distinctive advantages and drawbacks. New applications require high spatial and temperature resolution<sup>5</sup> in combination with large fields of view, and many samples can only be studied with noncontact methods.

Thermorefectance is an interesting technique for non-contact, high spatial resolution temperature imaging applications since the illumination wavelength can be chosen to allow a submicrometer spatial resolution unavailable from diffraction-limited standard IR imaging. Thermorefectance imaging measures the fractional change in the sample's reflectivity  $\Delta R/R$  ( $\Delta R$  refers to the change in reflectivity and  $R$  is the total reflectivity) in response to surface temperature variations  $\Delta T$ :

$$\frac{\Delta R}{R} = \frac{1}{R} \frac{\partial R}{\partial T} \Delta T \equiv \kappa \Delta T. \quad (1)$$

Knowledge of the material-dependent thermorefectance coefficient  $\kappa$  (typical values range from  $10^{-6}$  to  $10^{-3}$  K<sup>-1</sup>) enables the calculation of  $\Delta T$  from the measured  $\Delta R/R$ . Since the signal is small, lock-in techniques are used to obtain high-temperature resolution and to filter out the effects of slow temperature drifts in the measurement.

Although single-point measurements and scanning techniques have been the historically prevalent methods for thermorefectance, diode arrays connected to multiple lock-in amplifiers<sup>6</sup> and charge-coupled devices<sup>7-9</sup> (CCDs) have also been used. CCD detectors are particularly attractive for their high pixel count, low cost, and commercial availability. There is substantial literature available on CCD thermorefectance imaging, and there have been several recent advances in the thermorefectance field.<sup>7-14</sup>

However, the finite bit-depth of CCD cameras is sometimes thought to set a limit on the dynamic range of the thermorefectance measurements,<sup>15</sup> constraining the

smallest measurable signal amplitude in each CCD pixel to 1 bit and making it impossible to attain thermal resolutions comparable to that of traditional IR thermography or single-point photodetector measurements. This would mean that the smallest measurable temperature difference (that corresponding to the 1 bit quantization threshold) in a 12 bit CCD camera for a favorable thermoreflectance coefficient (e.g., doped Si, 525 nm,  $\kappa=2.20 \times 10^{-4} \text{ K}^{-1}$ ) is  $\Delta T=1/(2^{12}\kappa)=1.1 \text{ K}$ . It has also been separately suggested that the dynamic range is limited by the maximum number of electrons in a full CCD camera well, with a corresponding dynamic range of 100 dB.<sup>6</sup> It is the aim of this work to show that one can do better than these limits and to provide a quantitative theoretical description of the CCD thermoreflectance technique, like that which can be found for other imaging techniques.<sup>16</sup> We rely on lock-in detection and additive dither, a well-established tool of the signal processing and stochastic signal community,<sup>17–22</sup> to surpass this limit by more than 2 orders of magnitude, and we compare the theory to measurements for signals above and below the quantization threshold. The price one must pay for this enhanced accuracy is a longer duration measurement, since significant averaging (e.g.,  $10^3$ – $10^5$  measurement iterations) may be necessary to obtain a desired signal-to-noise ratio. We check the accuracy of the technique with a measurement of small (subquantization) heating signals in a doped silicon resistor, comparing the results to an independent temperature measurement using the well-established  $3\omega$  technique.

## 2. MEASUREMENT MODEL

The thermoreflectance apparatus used (Fig. 1) was a homodyne measurement setup similar to that used by others in the field,<sup>8</sup> and is shown in Fig. 1. The probe beam from a light-emitting diode (LED) provided steady illumination on the surface of the test device. Reflected LED light from the surface of the test device was collected through a microscope objective and imaged onto a video graphics CCD array ( $652 \times 494$  pixels, Opteon, Cambridge, Mass.). The optical spatial resolution was determined by measuring the full width at half maximum of a thin wire.<sup>23</sup> We have shown elsewhere that, in quantitative agreement with the Sparrow criterion,<sup>24</sup> an optical spatial resolution of  $225 \pm 10 \text{ nm}$  is attainable using 467 nm LED light, and a  $100\times$ ,  $\text{NA}=0.8$  microscope objective.<sup>23</sup> Because the spatial resolution scales linearly with the wavelength chosen for the measurement, a shorter wavelength can resolve a smaller distance. However, depending on the thermoreflectance spectrum of the material to be imaged (and practical constraints such as the spectral sensitivity of the CCD camera and the availability of a given wavelength for illumination), it may be more profitable to use a slightly longer wavelength. Because this work was focused on attaining high thermal resolution, we chose wavelengths with large thermoreflectance coefficients for each imaged material: 525 nm (green) for the silicon-based devices and 467 nm (blue) for measurements on gold.

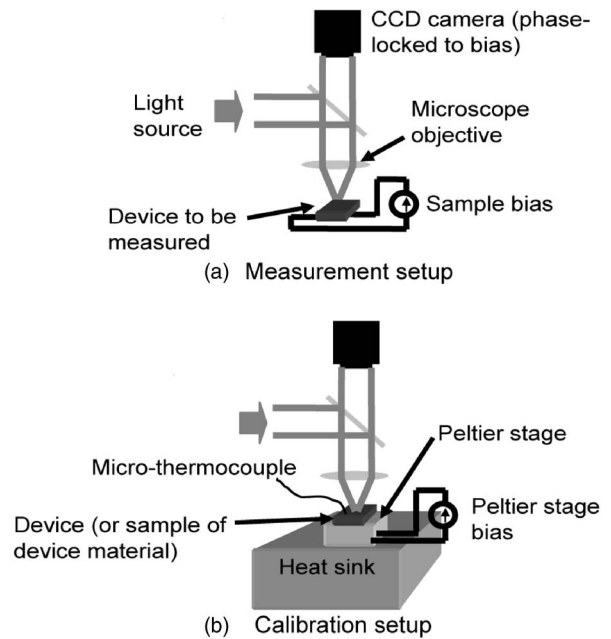


Fig. 1. Thermoreflectance measurement setup. (a) Measurement configuration relies on a CCD camera whose image acquisition is phase locked to a source of thermal excitation in the device of interest. A LED provides a source of illumination, and a microscope objective is used to obtain the desired spatial resolution. (b) Calibration configuration is used to obtain the thermoreflectance coefficients for a material of interest whose temperature is modulated on a Peltier stage.

The test device typically has a planar surface (e.g., a microelectronic die) whose temperature can be modulated by some means at a frequency  $\omega$ . In a resistive sample this can be obtained by joule heating from a sinusoidal current modulated at a frequency  $\omega/2$ . The principle of the measurement is that the periodic temperature modulation in the test device causes a small corresponding change in its reflectance according to Eq. (1), and the resulting modulation in the reflected signal is detected with the CCD array. If the thermoreflectance coefficients of the imaged materials are measured or known,<sup>4</sup> then the temperature distribution in the image can be backed out. Figure 1(b) shows the method used for measurement of the thermoreflectance calibration coefficient. The temperature of the test device (or a sample of the same material as the test device) is simultaneously measured using a micro-thermocouple and the thermoreflectance setup. The temperature of the sample can be uniformly modulated using a commercial Peltier stage. We note that the calibration measurement is best performed at lower magnification to avoid any spurious mechanical signal from the thermal expansion and contraction of the sample and the TE stage.<sup>7</sup> It is crucial to use an illumination wavelength that is identical for both the calibration and the subsequent measurement, as the thermoreflectance response of materials can vary significantly over the visible spectrum and between materials.

In the camera, the charge in each of the CCD pixels is read out using a high-speed 12 bit analog-to-digital (A-to-D) converter at frame rates up to 80 Hz, and the resulting images are captured onto a computer. The camera is phase locked and triggered to take pictures at four times

the thermal excitation frequency, integrating the resulting CCD counts into four image buffers corresponding to each of the trigger phases. The magnitude and phase of the modulated light is found using a procedure based on a four-point discrete Fourier transform (the so-called four-bucket technique).<sup>25</sup> Because the camera is phase locked onto the chosen thermal excitation frequency, each of the pixels in the CCD camera is effectively performing a separate lock-in measurement on the image.<sup>26</sup> Thus any noise away from the frequency of interest (and also away odd multiples of the frequency, which are aliased down to the measurement frequency) is rejected, greatly enhancing the signal-to-noise ratio of the measurement.

The four-bucket technique requires that four images be acquired per period  $T$  of the sample modulation and summed pixel by pixel over a large number  $N$  of iterations to obtain the four measured image buffers  $I_k(x, y)$ :

$$I_k(x, y) = \sum_{i=1}^N \left[ \left( \frac{4}{T} \int_{(4i+R)T/4}^{(4i+k+1)T/4} (c(x, y) + \Delta(x, y) \cos(\omega t + \phi(x, y) + \psi)) dt \right) + d(x, y) \right], \quad k \in \{1, 2, 3, 4\}. \quad (2)$$

At each point, we assume the image consists of a constant part  $c(x, y)$  representing the time independent background reflection and a varying part  $\Delta(x, y)$  corresponding to the (small) modulation of the image due to the thermoreflectance signal at frequency  $\omega = 2\pi/T$ . Here  $\phi(x, y)$  is the phase of each pixel due to the thermal modulation, and  $\psi$  is an arbitrary uniform phase shift that can be included to account for any overall delay between the modulation signal and the trigger or the image capture. The integral in Eq. (2) describes the collection of counts in the CCD camera while the shutter is open. For simplicity, and to maximize the signal intensity, the collection time for each image  $I_k$  is assumed here to be the full quarter period ( $T/4$ ). The term  $d(x, y)$  is a noise term containing the lumped effects of all of the noise sources associated with the measurement before the quantization step of the CCD camera, which is indicated in the equation by the floor brackets  $\lfloor \cdot \rfloor$ . From now on, the explicit dependence of all quantities on the pixel position  $(x, y)$  will be omitted for simplicity, since the information from each pixel is processed identically.

When the effects of noise and quantization in Eq. (2) are ignored, it is straightforward to show that the following expressions hold for the magnitude and phase in terms of the  $I_k$ :

$$\left| \frac{\Delta R}{R} \right|_{\text{ideal}} = \frac{\pi}{\sqrt{2}} \frac{\sqrt{(I_1 - I_3)^2 + (I_2 - I_4)^2}}{I_1 + I_2 + I_3 + I_4} = \frac{\Delta}{c}, \quad (3)$$

$$\phi_{\text{ideal}} = \arctan\left(\frac{I_1 - I_2 - I_3 + I_4}{I_1 + I_2 - I_3 - I_4}\right) - \psi = \phi. \quad (4)$$

These expressions are similar to those used in previous work<sup>8</sup> except for differences of convention resulting from how the  $I_k$  were defined in Eq. (2).

All of the pixel noise associated with the photodetection process is included in the random variable  $d$ , which is as-

sumed to have a Gaussian probability distribution function (pdf) with zero mean and variance  $\sigma_d^2$ . While its units are CCD counts, fractional values of  $d$  are allowed since the noise is present before the quantization. The standard deviation of the noise can be written

$$\sigma_d = \alpha\sqrt{c} + \beta. \quad (5)$$

The signal dependent term (with the prefactor  $\alpha$ ) models the shot noise of the incoming photons, and therefore scales with the square root of the signal. The true pdf describing photon shot noise is actually the Poisson pdf, but for the large numbers of photogenerated electrons present in these measurements ( $\gg 1000$ ) and for the purpose of this analysis, the Poisson distribution may be approximated by a Gaussian pdf.<sup>27</sup> The signal independent term ( $\beta$ ) models the detector noise that does not depend on the incoming signal intensity (e.g., thermal readout noise).<sup>28,29</sup> Both  $\alpha$  and  $\beta$  are measurable constants for a particular camera, and it will be described later how to measure them.

During the measurement, the signal and noise are quantized by the camera and stored in the buffers,  $I_k$ . In general, this is a nonlinear process whose output depends nontrivially on the signal. However, it is known that if the standard deviation of the noise source in the incoming signal is larger than the quantization bin size of the camera ( $\sigma_d > 1$ ), the error due to quantization rapidly becomes uncorrelated with the input signal.<sup>21</sup> This means that the effects of quantization noise can be represented as an additive (uncorrelated) white noise process of standard deviation  $\sigma_{\text{quant}} = 1/\sqrt{12}$ , a familiar result from the A-to-D signal processing literature.<sup>30</sup> The quantization noise then can be absorbed into the  $\beta$  coefficient in the expression for the pixel noise.

To complete the mathematical description of the measured signal and noise, the fundamental noise sources [Eq. (5)] and the signal [Eq. (2)] are propagated through Eqs. (3) and (4) to obtain a pdf for the measured quantities of interest.

### 3. MEASUREMENT OUTPUT: THEORY AND EXPERIMENT

Each of the  $I_k$  in Eq. (2) are the sum of  $N$  successive exposures with uncorrelated noise  $d$ , and can hence be described by Gaussian pdfs with mean  $\mu_k$  and variance  $N\sigma_d^2$ . The mean  $\mu_k$ 's contain all of the desired information about the temperature oscillation and are easily calculated from Eq. (2):

$$\mu_k = N \left( c - \frac{4\Delta}{\pi\sqrt{2}} \left( \cos\left(\frac{\pi k}{2} - \frac{\pi}{4}\right) \sin(\phi + \psi) + \sin\left(\frac{\pi k}{2} - \frac{\pi}{4}\right) \cos(\phi + \psi) \right) \right). \quad (6)$$

We note that this result can be easily generalized for the case when the shutter of the CCD is open for less time than the full quarter period assumed in Eq. (2).

To calculate the probability distribution of the observed output magnitude and phase, the pdf of the noise is propagated through a standard expression for the ther-

moreflectance magnitude [Eq. (3)]. For thermoreflectance measurements, the constant background reflectance is far larger than both the noise and the signal ( $\mu_k \approx Nc \gg \sqrt{N\sigma_d^2}$ ). Hence the effects of the noise in the denominator of Eq. (3) can be ignored. Equation (3) can therefore be rewritten in terms of two new random variables,  $A$  and  $B$ :

$$\left| \frac{\Delta R}{R} \right| \equiv \sqrt{\left[ \frac{\pi I_1 - I_3}{\sqrt{2} \sum_k \mu_k} \right]^2 + \left[ \frac{\pi I_2 - I_4}{\sqrt{2} \sum_k \mu_k} \right]^2} = \sqrt{A^2 + B^2}. \quad (7)$$

Here  $A = (\pi/\sqrt{2})(I_1 - I_3)/(4Nc)$  is described by a Gaussian pdf with mean  $\mu_A = (\pi/\sqrt{2})(\mu_1 - \mu_3)/(4Nc)$ , and  $B = (\pi/\sqrt{2})(I_2 - I_4)/(4Nc)$  is described by a Gaussian pdf with mean  $\mu_B = (\pi/\sqrt{2})(\mu_2 - \mu_4)/(4Nc)$ . Both  $A$  and  $B$  have a variance given by

$$\sigma^2 = \frac{\pi^2 2N\sigma_d^2}{2(4Nc)^2} = \frac{\pi^2 \sigma_d^2}{16Nc^2}.$$

The resulting pdf for  $r = |\Delta R/R|$  is the so-called Rician (or Rice)<sup>31</sup> distribution

$$p_r(r) = \frac{r}{\sigma^2} \exp\left(-\frac{r^2 + \mu_A^2 + \mu_B^2}{2\sigma^2}\right) I_0\left(r \frac{\sqrt{\mu_A^2 + \mu_B^2}}{\sigma^2}\right), \quad (8)$$

where  $I_0$  denotes the zeroth-order modified Bessel function. We note that in the limit of low noise (small  $\sigma$ ) and perfect quantization (vanishingly small bit size), the Rician collapses to a delta function distribution centered on the value

$$\left| \frac{\Delta R}{R} \right|_{\text{ideal}} = \sqrt{\mu_A^2 + \mu_B^2} = \frac{\Delta}{c}, \quad (9)$$

confirming the right-most equality in Eq. (3).

In general, all of the moments of a pdf are necessary for the complete characterization of its statistics, but here we found that the number of iterations needed to measure a temperature signal to a given accuracy can be adequately predicted using the first two moments. It is straightforward to calculate the first and second moments of Eq. (8), and one finds

$$\begin{aligned} E\left[\frac{\Delta R}{R}\right] &= \sqrt{2}\sigma \exp\left(-\frac{\mu_A^2 + \mu_B^2}{2\sigma^2}\right) \left[ \frac{1}{2} \sqrt{\pi} \left(1 + \frac{1}{2} \frac{\mu_A^2 + \mu_B^2}{\sigma^2}\right) \right. \\ &\quad \times \exp\left(\frac{\mu_A^2 + \mu_B^2}{4\sigma^2}\right) I_0\left(\frac{\mu_A^2 + \mu_B^2}{4\sigma^2}\right) \\ &\quad \left. + \frac{\sqrt{\pi}(\mu_A^2 + \mu_B^2)}{4\sigma^2} \exp\left(\frac{\mu_A^2 + \mu_B^2}{4\sigma^2}\right) I_1\left(\frac{\mu_A^2 + \mu_B^2}{4\sigma^2}\right) \right], \end{aligned} \quad (10)$$

$$E\left[\left(\frac{\Delta R}{R}\right)^2\right] = 2\sigma^2 + \mu_A^2 + \mu_B^2. \quad (11)$$

Here  $I_1$  refers to the first-order modified Bessel function. From these, one can find the standard deviation of  $\Delta R/R$

(the typical measure of experimental random error) in terms of the original fundamental pixel noise terms:

$$\sigma_{\Delta R/R}(c, N) = \sqrt{E\left[\left(\frac{\Delta R}{R}\right)^2\right] - E\left[\frac{\Delta R}{R}\right]^2}. \quad (12)$$

One can also find the offset error, the difference between the signal that is actually present and the mean of the measured signal:

$$\varepsilon_{\text{offset}} \equiv E\left[\frac{\Delta R}{R}\right] - \frac{\Delta R}{R}\bigg|_{\text{ideal}} = E\left[\frac{\Delta R}{R}\right] - \sqrt{\mu_A^2 + \mu_B^2}. \quad (13)$$

The offset error fundamentally arises from the squaring of the zero-mean Gaussian noise in Eq. (7). For insufficient measurement duration, this can be a large source of error, unless it is specifically subtracted.

With Eqs. (12) and (13), the practical descriptions of the measurement and its statistical accuracy are complete. For a specified illumination level (given by  $c$ ), and a target thermal signal magnitude (given by  $\Delta$ ), one can compute the number of iterations  $N$  needed to obtain a given accuracy, as described by  $\varepsilon_{\text{offset}}$  and  $\sigma_{\Delta R/R}$ . The only inputs to the theory are the camera-dependent parameters  $\alpha$  and  $\beta$  of Eq. (5).

To extract  $\alpha$  and  $\beta$  for a given camera, one can take measurements of the background thermoreflectance of a uniformly reflecting background (with no thermal modulation) for a few different values of  $c$  and  $N$ . Areas of the image can be used to obtain the pixel variances, eliminating the need for an ensemble of measurements at one intensity level and greatly speeding the characterization. Using the limit of Eq. (12) for no thermal modulation ( $\mu_A = \mu_B = 0$ ), one can find a simple expression for the standard deviation of  $\Delta R/R$ :

$$\begin{aligned} \sigma_{\Delta R/R}(c, N) &= \sqrt{E\left[\left(\frac{\Delta R}{R}\right)^2\right] - E\left[\frac{\Delta R}{R}\right]^2} \\ &= \frac{\pi}{4} \sqrt{2 - \frac{\pi}{2} \frac{1}{\sqrt{Nc}} (\alpha\sqrt{c} + \beta)}. \end{aligned} \quad (14)$$

Using this expression and our measurements of  $\sigma_{\Delta R/R}(c, N)$  for 25 adjacent pixels, we extract  $\alpha = 0.207$  and  $\beta = 7.65$  for our camera. The 25 pixels formed a  $5 \times 5$  box in the image, large enough to obtain statistics from but small enough to ensure temperature and reflectance uniformity in the region of interest. The camera pixel noise can also be measured using more standard techniques.<sup>29,32</sup> These values also confirm that the noise was larger than the quantization bin size, justifying the use of linear signal theory with an additive noise source to model the quantization process.

To compare the results of the theory developed above with measurements, sets of thermoreflectance data were taken on a smooth gold surface whose temperature was modulated with an external current bias. Using 25 adjacent pixels in an area of uniform and constant-amplitude temperature modulation, the mean (measured signal) and standard deviation (noise) of the detected thermoreflec-

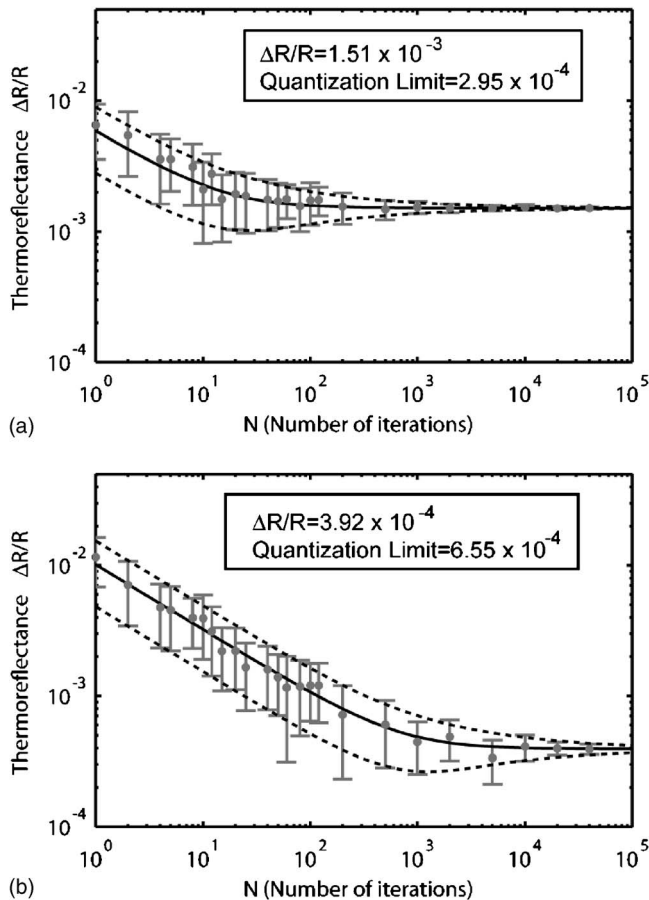


Fig. 2. Thermoreflectance measurements (gray) and theory (black) plotted against the number of iterations for thermal signals (a) above and (b) below the quantization threshold. For each measurement, 25 pixels are used to calculate the mean response and the 1-sigma error bars. Solid curve, theoretically predicted mean response; dotted curves, theoretically predicted 1-sigma error limits. Theory and experiment agree quantitatively in both cases.

tance magnitude were calculated from the images  $I_1$ ,  $I_2$ ,  $I_3$ , and  $I_4$  using Eqs. (3) and (4). This was done for a signal above and below the quantization threshold of the camera. The dependence of the measured signal and the noise on the amount of averaging (that is, on the number of iterations  $N$ ) is of crucial importance for practical experiments, and can be computed directly from the theory above [Eqs. (14) and (13)]. Also of interest is experimental confirmation that the theory works equally well both above and below the quantization threshold.

Figure 2 plots the measured thermoreflectance signals from the two data sets as the number of measured iterations is increased. In Fig. 2(a), the magnitude of the thermoreflectance signal is above the quantization threshold, whereas in Fig. 2(b), the signal is below the quantization threshold. The model and the experiment agree well for signals above and below the quantization limit, for both the mean and the standard deviation of the measured signal. In each case, for sufficient averaging (large  $N$ ) the mean of the measurements converges to a stable value of the measured thermoreflectance. As expected, for a smaller signal more averaging is required, and insufficient averaging (small  $N$ ) gives rise to both random error

and offset error. It is also clear from Fig. 2(b) that with enough averaging, signals smaller than one bit of quantization can be resolved. This is fundamentally due to the presence of noise on the signal before the quantization process.

Once the camera noise parameters  $\alpha$  and  $\beta$  are known, this model can be used to predict the duration of the measurement (the number of iterations  $N$ ) needed to obtain a given measurement precision. A similar noise model based on the same parameters can be developed for the phase of the thermoreflectance and is presented in Appendix A.

#### 4. MILLIKELVIN SUB-QUANTIZATION-LIMIT MEASUREMENT: CHIP RESISTOR

So far, it has been shown that the thermoreflectance measurement converges towards a stable value after sufficient averaging. To experimentally confirm that meaningful temperature signals smaller than the least significant bit of the quantizer can be measured with accuracy, we measured the linear temperature dependence of a boron-doped Si resistor with varying input heating power. The current into the resistor was modulated sinusoidally around zero at 6 Hz, resulting in a temperature (and reflectance) signal at 12 Hz due to joule heating. The CCD camera trigger was locked to the reflectance signal at 48 Hz, and a  $10\times$ ,  $\text{NA}=0.28$  objective was used. Using the standard calibration method [Fig. 1(b)], the thermoreflectance coefficients for 525 nm green light in the boron-doped Si ( $\kappa=2.20\times 10^{-4}\text{ K}^{-1}$ ) and the undoped Si ( $\kappa=1.36\times 10^{-4}\text{ K}^{-1}$ ) were measured in a separate low magnification ( $20\times$ ,  $\text{NA}=0.42$ ) measurement on convenient test areas located on the same wafer. (Separate measurements were made to ensure that the switching between the  $20\times$  and  $10\times$  objectives did not result in differing thermoreflectance coefficients.) The calibration constant for the doped Si could be used to extract the mean temperature in the resistor from the raw thermoreflectance profile (inset to Fig. 3). The mean level of camera counts for the measurements was  $c=1550$ . The thermoreflectance signal at the quantization threshold was  $\Delta R/R=1$

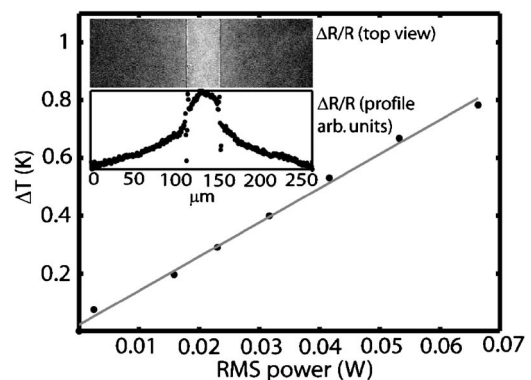


Fig. 3. For a resistor, the amplitude of the temperature change  $\Delta T$  is expected to be proportional to the electrical input power  $P$ . Data follow the expected linear trend, confirming that temperature levels smaller than one quantization bit (2.93 K) can be measured reliably. Inset, thermoreflectance image of the  $p$ -doped Si resistor on the Si substrate, along with the thermoreflectance profile across the resistor.

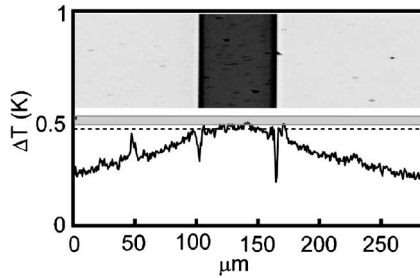


Fig. 4. Average value (dotted black line) of the measured temperature profile (solid black curve) is close to an independent measurement of the resistor's temperature using the  $3\omega$  method. Shaded gray box indicates the  $\pm$  one sigma confidence interval for the  $3\omega$  measurement. Inset, micrograph of the region of interest, where the dark vertical stripe is the resistor. Two thermoreflectance coefficients (for doped and undoped Si) were separately measured to reconstruct the temperature profile inside and outside the resistor.

count/1550 counts, and in the Si resistor this corresponded to a temperature of  $\Delta R/R/\kappa=2.93$  K.

The data presented in Fig. 3 clearly show the expected linear dependence of the measured temperature on the dissipated electrical power, even though all signals are measured well below the temperature corresponding to the quantization limit of the camera. For all but the smallest data point  $N=10^5$  iterations were used, resulting in a measurement time of 2.3 h per point. The temperature resolution is estimated to be 18 mK by calculating the standard deviation of the error from a linear fit to the points in Fig. 3.

An advantage of using this resistor geometry (photo shown in the inset of Fig. 4) was that the accuracy of the calibration procedure could be independently confirmed using a  $3\omega$  measurement of the resistor's average temperature. The  $3\omega$  technique relies on the doped silicon's resistance changing slightly with temperature. Joule heating, from a sinusoidal input current at a frequency  $\omega$ , causes the resistor's temperature and resistance to change at a frequency of  $2\omega$ . From the resulting additional voltage signal at a frequency of  $3\omega$ , the mean temperature of the resistor can be extracted.

The temperature profile in Fig. 4 was calculated by scaling the raw thermoreflectance image (an example of which was shown in the inset to Fig. 3) by the measured thermoreflectance coefficients inside and outside the resistor. We note that as a result, the unphysical-appearing jump that can be observed in the thermoreflectance profile at the edge of the resistor in Fig. 3 is not present in the temperature profile of Fig. 4. The results of the  $3\omega$  measurement at the same bias are shown as the shaded band in Fig. 4. The top and bottom edges of the band are the plus and minus one sigma confidence intervals of the  $3\omega$  measurement, respectively. The average temperatures from the  $3\omega$  measurement (center of shaded band) and from the thermoreflectance profile (dotted line) differ by 38 mK, or approximately 7.8%.

We note that in separate measurements performed on gold and presented elsewhere,<sup>23</sup> the thermoreflectance coefficient was  $\kappa=3.3\times 10^{-4}$  K<sup>-1</sup>, allowing for an even higher temperature resolution of 10 mK for the parameters mentioned above. Also in that previous work, a tem-

perature resolution of 1.5 mK was obtained through spatial averaging at 900 nm spatial resolution.

## 5. DISCUSSION AND CONCLUSION

It is important to consider any potential sources of error not accounted for in the theory presented above. The question arises: is there a fundamental limit to the accuracy of the technique, provided one is willing to average for long enough to reduce the effects of random noise?

The effects of any slow temperature drifts do not appear directly in the measured thermoreflectance signal, since the lock-in measurement rejects changes in the reflectance occurring at frequencies less than the detection frequency  $\omega=2\pi/T$ . Drifts may still affect the position of components in the measurement image train, but they are generally easily recognized by the resulting blurring of the image. Such drifts may be mitigated with good environmental control, but are a definite concern for the longer measurements that may be required for high thermal resolution. For certain devices that degrade with thermal cycling, the stability of the device under test may limit the measurement time and the subsequent attainable thermal resolution. We note that drift of the illumination source intensity does not generally adversely affect the measurement because the measured thermoreflectance is the ratio of  $\Delta R$  to  $R$ , both of which would change by the same factor. (In fact, depending on the camera used, slowly varying the illumination somewhat during the measurement might improve the accuracy of the measurement by further reducing any systematic error due to camera nonlinearity.)

However, as with other subquantization dithered measurements, imperfections in the A-to-D converter may fundamentally limit the accuracy of the CCD thermoreflectance measurements presented here. The errors due to imperfect spacing of the quantization bins of the A-to-D transfer function are traditionally divided into differential nonlinearity (DNL) and integral nonlinearity (INL).<sup>31</sup> The DNL describes the difference between the width of a given quantization bin and the ideal quantization bin size, whereas the INL describes the difference of the A-to-D transfer function from an ideal straight-line fit. Both errors are systematic and do not decrease with time averaging, and so they can potentially distort the temperature signal measured with the camera regardless of how long the measurement is run. Figure 5 shows an example of an imperfect quantization spectrum. The input signal (potentially anywhere on the  $x$  axis) is mapped to a discrete value on the  $y$  axis during the quantization process. The imperfection we refer to lies in the variation of the quantization bin size (the width of the steps in the staircase) from its ideal size. Shown in the insets of the figure are the size of the DNL error and INL error over 256 quantization bins. Such plots can also generally be found in the specification sheets offered by the manufacturers of A-to-D converters.

For a thermoreflectance measurement where the errors in the quantization levels are locally uncorrelated with one another, the DNL will be the main source of error. According to the manufacturer's specifications, the standard deviation of the DNL error for our camera's A-to-D con-

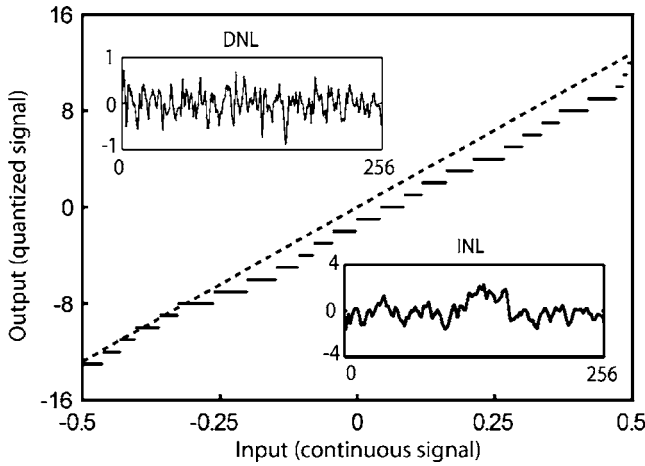


Fig. 5. Example of an imperfect A-to-D quantizer. Presence of unequal bin widths simulates the quantizer's nonlinearity error. In this case, a DNL of 0.35 quantization steps has been assumed. Top inset, plot of the DNL error over 256 bins of the A-to-D converter; bottom inset, similar plot of the INL error.

verter is in the 0.2 to 0.5 range (in units of quantization levels). This might appear to severely limit the effectiveness of the time averaging relied upon to obtain high accuracy. But once again, the dither present in the signal decreases the importance of these errors. Since many quantization bins will be used to measure the signal, the errors from individual quantization bins are averaged out.

By running a simulated measurement of a small thermal signal with a (randomly generated) imperfect quantizer, we can estimate the effects of imperfect quantization on the accuracy of the measurement. We used a signal that was 5% of the quantization bin with a random noise whose standard deviation was 10 quantization bins in magnitude (of the order of what was measured in our camera). We simulated the lock-in measurement on this signal for  $2^{20}=1,048,576$  periods of the signal to reduce any random (statistical) error. The simulation was run 100 times, each with a different imperfect quantizer with a DNL of 0.35 (consistent with the specifications of our camera), in order to get an ensemble average of the systematic error. One instance of the imperfect quantizer is shown in Fig. 5. The result of the simulation was that the residual systematic error due to the detector nonlinearity was 4.6% of the signal. For the resistor measurements shown in Fig. 3, this corresponds to a systematic error of 6.7 mK due to A-to-D quantization error.

In summary, we have shown that the dynamic range of CCD-based modulation experiments is not principally limited by the finite bit depth of the detector. Stochastic resonance enables the successful measurement of signals far smaller than the least significant bit of the detector. We present the first complete theory (with experimental confirmation) of the measurement process, allowing for the explicit calculation of the signal-to-noise ratio for a given set of experimental conditions. We also present a check on the validity of the calibration process using the  $3\omega$  technique, and we suggest that imperfections in the A-to-D quantization may give rise to systematic error that ultimately sets a lower limit on measurement accuracy.

## APPENDIX A: PHASE MEASUREMENT THEORY

From the standpoint of temperature measurement, knowledge of the pdf of the measured thermoreflectance signal is sufficient, but for more general applications of the thermoreflectance technique, information on the phase distribution can be useful. Here we extend the analysis to the phase,  $\phi$ .

Because of how we have defined the phase [Eq. (2)], it is convenient to define new random variables in terms of  $A$  and  $B$  from Eq. (7) according to

$$Y \equiv A - B, \quad p_Y = \mathcal{N}(\mu_A - \mu_B, 2\sigma^2) = \mathcal{N}(\mu_Y, \sigma_\phi^2),$$

$$X \equiv A + B, \quad p_X = \mathcal{N}(\mu_A + \mu_B, 2\sigma^2) = \mathcal{N}(\mu_X, \sigma_\phi^2), \quad (\text{A1})$$

such that

$$\phi = \arctan\left(\frac{Y}{X}\right) - \Psi = \arctan\left(\frac{I_1 - I_2 - I_3 + I_4}{I_1 + I_2 - I_3 - I_4}\right) - \Psi. \quad (\text{A2})$$

$Y$  and  $X$  so chosen can be shown to be independent by writing the joint pdf for  $A$  and  $B$ , substituting variables, and then factoring  $p_{X,Y}(X,Y)=[p_X(X)][p_Y(Y)]$ . By writing the phase as in Eq. (A2), it is recognizable as the angle formed by the vectorial sum of the independent Gaussian random variables  $X$  and  $Y$ . The joint Gaussian pdf for  $X$  and  $Y$  is given by

$$p_{X,Y}(X,Y) = \frac{1}{2\pi\sigma^2} \exp\left(-\frac{(X - \mu_X)^2 + (Y - \mu_Y)^2}{2\sigma^2}\right). \quad (\text{A3})$$

After changing variables according to  $X=r \cos \phi$  and  $Y=r \sin \phi$ , one can write a joint pdf for the new variables:

$$p_{r,\phi}(r,\phi) = \frac{r}{2\pi\sigma^2} \exp\left(-\frac{1}{2\sigma^2}[(r \cos \phi - \mu_X)^2 + (r \sin \phi - \mu_Y)^2]\right). \quad (\text{A4})$$

To obtain an expression for the pdf of the phase, we integrate Eq. (A4) over  $r$ , where  $r \equiv \sqrt{X^2 + Y^2}$ . One finds

$$p_\phi = \frac{1}{2\pi} \exp\left(-\frac{\mu_X^2 + \mu_Y^2}{2\sigma_\phi^2}\right) + \frac{\sqrt{\mu_X^2 + \mu_Y^2} \cos(\phi - \theta)}{2\sqrt{2}\pi\sigma_\phi} \times \exp\left(-\frac{(\mu_X^2 + \mu_Y^2)\sin^2(\phi - \theta)}{2\sigma_\phi^2}\right) \times \left(1 + \operatorname{erf}\left(\frac{\sqrt{\mu_X^2 + \mu_Y^2} \cos(\phi - \theta)}{2\sigma_\phi}\right)\right). \quad (\text{A5})$$

Here  $\tan \theta \equiv \mu_Y/\mu_X$ .

The pdf has the form of a uniform term that exponentially decreases with an increasing signal-to-noise level, and a second term peaked around the angle  $\theta$ . When the noise  $\sigma_\phi$  is allowed to approach zero, the pdf approaches zero everywhere except around  $\phi - \theta = 0$ , where it diverges. Thus the phase pdf converges to the value expected for the case of no noise [Eq. (4)].

With the full expression for the phase probability distribution function, the phase noise can be calculated by taking moments of the pdf. Due to the complexity of the expressions, this is best performed by numerically integrating Eq. (A5).

## ACKNOWLEDGMENTS

This work was supported by the National Science Foundation and an Office of Naval Research Multidisciplinary University Research Initiative program.

Dietrich Lürßen's present address is Oxford Gene Technology, Oxford OX5 1PF, U.K.

P. Mayer's e-mail address is pmayer@mit.edu.

## REFERENCES

- J. Marek and Y. E. Strausser, "Correlation of thermal-wave imaging to other analysis methods," *Appl. Phys. Lett.* **44**, 1152–1154 (1984).
- O. Breitenstein, M. Langenkamp, F. Altmann, D. Katzer, A. Lindner, and H. Eggers, "Microscopic lock-in thermography investigation of leakage sites in integrated circuits," *Rev. Sci. Instrum.* **71**, 4155–4160 (2000).
- K. Luo, Z. Shi, J. Varesi, and A. Majumdar, "Sensor nanofabrication, performance, and conduction mechanisms in scanning thermal microscopy," *J. Vac. Sci. Technol. B* **15**, 349–360 (1997).
- M. Cardona, *Modulation Spectroscopy*, Solid-State Physics, Supplement 11 (Academic, 1969).
- D. Cahill, K. Goodson, and A. Majumdar, "Thermometry and thermal transport in micro/nanoscale solid-state devices and structures," *J. Heat Transfer* **124**, 223–241 (2002).
- J. Christofferson and A. Shakouri, "Thermoreflectance based thermal microscope," *Rev. Sci. Instrum.* **76**, 24903–24909 (2005).
- S. Dilhaire, S. Grauby, and W. Claeys, "Calibration procedure for temperature measurements by thermoreflectance under high magnification conditions," *Appl. Phys. Lett.* **84**, 822–824 (2004).
- S. Grauby, B. C. Forget, S. Hole, and D. Fournier, "High resolution photothermal imaging of high frequency phenomena using a visible charge coupled device camera associated with a multichannel lock-in scheme," *Rev. Sci. Instrum.* **70**, 3603–3608 (1999).
- C. Filloy, G. Tessier, S. Hole, G. Jerosolimski, and D. Fournier, "The contribution of thermoreflectance to high resolution thermal mapping," *Sens. Rev.* **23**, 35–39 (2003).
- M. Fujinami, K. Toya, and T. Sawada, "Development of photothermal near-field scanning optical microscope photothermal near-field scanning optical microscope," *Rev. Sci. Instrum.* **74**, 621–623 (2003).
- G. Tessier, S. Hole, and D. Fournier, "Ultraviolet illumination thermoreflectance for the temperature mapping of integrated circuits," *Opt. Lett.* **28**, 875–877 (2003).
- G. Tessier, S. Hole, S. Grauby, and D. Fournier, "Quantitative thermal imaging by thermoreflectance using a CCD array," Presented at THERMINIC 2000, International Workshop No. 6, Budapest, September 24, 2000.
- S. Grauby, S. Dilhaire, S. Jorez, and W. Claeys, "Imaging setup for temperature, topography, and surface displacement measurements of microelectronic devices," *Rev. Sci. Instrum.* **74**, 645–647 (2003).
- C.-H. Ho, H.-W. Lee, and Z.-H. Cheng, "Practical thermoreflectance design for optical characterization of layer semiconductors," *Rev. Sci. Instrum.* **75**, 1098–1102 (2004).
- J. Christofferson and A. Shakouri, "Camera for thermal imaging of semiconductor devices based on thermoreflectance," in *Proceedings of the 20th Annual IEEE Semiconductor Thermal Measurement and Management Symposium* (IEEE, 2004), pp. 87–91.
- J. Philip and K. Carlsson, "Theoretical investigation of the signal-to-noise ratio in fluorescence lifetime imaging," *J. Opt. Soc. Am. A* **20**, 368–379 (2003).
- E. Balestrieri, P. Daponte, and S. Rapuano, "A state of the art on ADC error compensation methods," *IEEE Trans. Instrum. Meas.* **54**, 1–8 (2005).
- P. Carbone, "Quantitative criteria for the design of dither-based quantizing systems," *IEEE Trans. Instrum. Meas.* **46**, 656–659 (1997).
- P. Carbone and D. Petri, "Effect of additive dither on the resolution of ideal quantizers," *IEEE Trans. Instrum. Meas.* **43**, 389–396 (1994).
- L. Gammaitoni, P. Hanggi, P. Jung, and F. Marchesoni, "Stochastic resonance," *Rev. Mod. Phys.* **70**, 223–287 (1998).
- R. A. Wannamaker, S. P. Lipshitz, J. Vanderkooy, and J. N. Wright, "A theory of nonsubtractive dither," *IEEE Trans. Signal Process.* **48**, 499–516 (2000).
- J. Potzick, "Noise averaging and measurement resolution (or "A little noise is a good thing")," *Rev. Sci. Instrum.* **70**, 2038–2040 (1999).
- D. Luerssen, J. A. Hudgings, P. M. Mayer, and R. J. Ram, "Nanoscale thermoreflectance with 10 mK temperature resolution using stochastic resonance," in *Proceedings of the 21st Annual IEEE Semiconductor Thermal Measurement and Management Symposium* (IEEE, 2005), pp. 253–258.
- S. Inoué and K. R. Spring, *Video Microscopy: The Fundamentals*, 2nd ed. (Plenum, 1997).
- G. Busse, D. Wu, and W. Karpen, "Thermal wave imaging with phase sensitive modulated thermography," *J. Appl. Phys.* **71**, 3962–3965 (1992).
- O. Breitenstein and M. Langenkamp, *Lock-in Thermography: Basics and use for Functional Diagnostics of Electronic Components*, Springer Series in Advanced Microelectronics (Springer, 2003).
- W. M. Hubbard, "Approximation of a Poisson distribution by a Gaussian distribution," *Proc. IEEE* **58**, 1374–1375 (1970).
- J. Janesick, "CCD transfer method—standard for absolute performance of CCDs and digital CCD camera systems," *Proc. SPIE* **3019**, 70–102 (1997).
- Y. Reibel, M. Jung, M. Bouhifd, B. Cunin, and C. Draman, "CCD or CMOS camera noise characterization," *Eur. Phys. J.: Appl. Phys.* **21**, 75–80 (2003).
- A. V. Oppenheim, R. W. Schaffer, and J. R. Buck, *Discrete-Time Signal Processing*, Prentice Hall Signal Processing Series, 2nd ed. (Prentice Hall, 1999).
- C. F. Coombs, *Electronic Instrument Handbook*, 3rd ed. (McGraw-Hill, 2000).
- J. C. Mullikin, L. J. V. Vliet, H. Netten, F. R. Boddeke, G. v. d. Feltz, and I. T. Young, "Methods for CCD camera characterization," *Proc. SPIE* **2173**, 73–84 (1994).